International Journal of
Molecular Sciences

MDPI

Article

Influence of Te-Incorporated $LaCoO_3$ on Structural, Morphology and Magnetic Properties for Multifunctional Device Applications

Jhelai Sahadevan [1,†], P. Sivaprakash [2,†], S. Esakki Muthu [1,*], Ikhyun Kim [2,*], N. Padmanathan [1,3] and V. Eswaramoorthi [4]

[1] Department of Physics, Karpagam Academy of Higher Education, Coimbatore 641021, India; jhelaidev@gmail.com (J.S.); padmanmsc@gmail.com (N.P.)
[2] Department of Mechanical Engineering, Keimyung University, Daegu 42601, Republic of Korea; siva.siva820@gmail.com
[3] Micro-Nano System Centre, Tyndall National Institute, University College Cork, T12R5CP Cork, Ireland
[4] Department of Physics, Karpagam College of Engineering, Coimbatore 641032, India; physicseswar@gmail.com
* Correspondence: sanrajson@yahoo.com (S.E.M.); kimih@kmu.ac.kr (I.K.)
† These authors contributed equally to this work.

Abstract: A high perovskite activity is sought for use in magnetic applications. In this paper, we present the simple synthesis of (2.5% and 5%) Tellurium-impregnated-$LaCoO_3$ (Te-LCO), Te and $LaCoO_3$ (LCO) by using a ball mill, chemical reduction, and hydrothermal synthesis, respectively. We also explored the structure stability along with the magnetic properties of Te-LCO. Te has a rhombohedral crystal structure, whereas Te-LCO has a hexagonal crystal system. The reconstructed Te was imbued with LCO that was produced by hydrothermal synthesis; as the concentration of the imbuing agent grew, the material became magnetically preferred. According to the X-ray photoelectron spectra, the oxidation state of the cobaltite is one that is magnetically advantageous. As a result of the fact that the creation of oxygen-deficient perovskites has been shown to influence the mixed ($Te^{4+/2-}$) valence state of the incorporated samples, it is abundantly obvious that this process is of utmost significance. The TEM image confirms the inclusion of Te in LCO. The samples start out in a paramagnetic state (LCO), but when Te is added to the mixture, the magnetic state shifts to a weak ferromagnetic one. It is at this point that hysteresis occurs due to the presence of Te. Despite being doped with Mn in our prior study, rhombohedral LCO retains its paramagnetic characteristic at room temperature (RT). As a result, the purpose of this study was to determine the impacts of RT field dependency of magnetization (M-H) for Te-impregnated LCO in order to improve the magnetic properties of RT because it is a low-cost material for advanced multi-functional and energy applications.

Keywords: rhombohedral; hydrothermal synthesis; chemical reduction; oxygen deficiency; low spin state; ferromagnetism

Citation: Sahadevan, J.; Sivaprakash, P.; Esakki Muthu, S.; Kim, I.; Padmanathan, N.; Eswaramoorthi, V. Influence of Te-Incorporated $LaCoO_3$ on Structural, Morphology and Magnetic Properties for Multifunctional Device Applications. *Int. J. Mol. Sci.* **2023**, *24*, 10107. https://doi.org/10.3390/ijms241210107

Academic Editor: Andrzej Grzybowski

Received: 25 May 2023
Revised: 9 June 2023
Accepted: 12 June 2023
Published: 14 June 2023

1. Introduction

Perovskites are one of the most fascinating types of solid materials, exhibiting a wide range of physical events and characteristics. Extensive research has been conducted on ABO_3-type perovskites with the general formula $Ln_{1-x}A_xMO_3$ or $LnB_xM_{1-x}O_3$ (Ln-Lanthanides and M-dopant). For decades, researchers have been intrigued by nano crystallite magnetic cobaltite due to its outstanding magnetic and electric capabilities. Single-phase $LaCoO_3$ perovskite is a good example of ceramic materials and is utilised in essential applications such as ZrB_2 + 10 wt.% SiC for leading edges and nose cones in hypersonic vehicles and $LaCoO_3$ for solid oxide fuel cell cathodes [1]. A wide variety of

practical applications are made possible by many intrinsic perovskite materials features due to the continuous interaction between structure and properties. Ferroelectricity [2–4], semi-conductivity [5,6], superconductivity [5,6], piezoelectricity [7,8], thermoelectricity [9], colossal magnetoresistance, ferromagnetism [10], and half-metallic transport [11,12] are just some of the fascinating physical and chemical properties of perovskites. These oxides are increasingly being used in electronic and magnetic materials, automotive exhaust, water splitting catalysts, fuel cells, battery electrode materials [13], gas sensors, humidity sensors, microwave devices, high-density data storage, magnetic ferrofluids, magnetic switches, MRI, high-frequency, and power devices are among the applications for these materials [2]. As demonstrated by the discovery of superconductivity in $Na_{0.3}CoO_2.1.3H_2O$, the fact that cobalt cations can assume multiple oxidation and spin states is the root cause of the wide range of observable physical features of cobaltites [14]. Specifically, the LCO perovskite is a classic example of thermally aided spin state transitions of trivalent cobalt [15,16]. Integration of divalent/trivalent or magnetic/nonmagnetic dopant ions into a lattice results in a drastic alteration of the structure and other properties defined by cation distribution. A dopant choice is needed to get the desired improvement in the unaltered perovskite cobaltite. In particular, the shift from paramagnetic (PM) to ferromagnetic (FM) at the Curie temperature (T_C) and the accompanying insulator–metal transition (T_{IM}) in the case of manganite and cobaltite have been known for some time. These include high conductivity, magnetic properties, excellent performance as a cathode or an anode, a high Seebeck coefficient, and various forms of oxygen vacancy ordering. The $LaCoO_3$ perovskite, for instance, is a famous example of thermally aided trivalent cobalt spin state transitions. It has a nonmagnetic insulator ground state with only low-spin (LS) Co^{3+}, but its magnetic susceptibility rises with temperature up to 100 K due to a transition from the LS to the intermediate-spin (IS) state. A second spin-state transition is then inferred from a shift in transport characteristics above 500 K from an activated regime (0.1 eV at 100 K) to a metallic regime (~1 mΩ cm), which corresponds to a conversion to high-spin (HS). The energetic proximity of the various Co^{3+} spin-states (LS, IS, and HS), as demonstrated by these two spin-state transitions, is also highlighted by the dramatic effect of a small amount of doping on physical attributes [17].

Ferroelastic materials having rhombohedral lattices are particularly fascinating. Stretching along one of the perovskite unit cell's four body diagonals distorts the parent cubic structure, causing ferro elasticity [18]. As previously reported, LCO is ferromagnetic at low temperatures [19], and B site incorporation increases the magnetic properties. The complicated interplay between the interatomic exchange interaction energy (Δ_{ex}) and the crystal field splitting energy (Δ_{cf}) controls the active spin crossover of Co ion's low and high spin states. A modest structural disruption brought on by strain can have a considerable effect since Δ_{cf} is particularly sensitive to changes in O-Co bond length and Co-O-Co bond angle [20,21].

Microwave heating, chemical co-precipitation, sol–gel auto-combustion [22], micro- and nano-emulsions, hydrothermal techniques, high-temperature breakdown, and reverse micelle have all been used to create cobaltite magnetic nanoparticles (NPs) [23–25]. The best way to produce $LaCoO_3$ is through hydrothermal synthesis because it is easy, cheap, and safe for the environment. One of the most important aspects of our study was the hydrothermal method, which allowed us to produce superior perovskite precipitates with the required stoichiometry and microstructure. Hydrothermal synthesis of LCO by L. Tepech-Carrillo et al., followed by a study of LCO structure at different calcination temperatures, is elaborated. However, they did not look into LCO or Te-LCO composites' structures or magnetic properties. Since Te (2.5% and 5%) in $LaCoO_3$ modifies the magnetic properties, we are attracted to studying the magnetic properties and structural analysis of this material [26]. Unlike our prior work, in which we discovered no change in paramagnetic states at RT when doping Mn into LCO, we found that the Te inclusion in LCO has impacted the RT magnetic characteristics of LCO crystals. Therefore, we set out to improve LCO's magnetic characteristics when it was exposed to RT. After discovering LT ferromagnetism

in Mn-doped LCO, we set out to investigate whether or not the same phenomenon would occur in Te-incorporated LCO.

2. Results and Discussion

2.1. Powder X-ray Diffraction (P-XRD) of Te-Incorporated $LaCoO_3$

For parent LCO and two different concentrations of 2.5% and 5%Te-LCO, the powder XRD patterns were taken. The standard single-phase crystallite perovskite structure of LCO (JCPDS 48-0123) can be used to assign all of the diffraction peaks of the prepared samples, proving that the perovskite structures are well preserved after Te incorporation, as shown in Figure 1. There were no peaks that could be attributed to impurities. Furthermore, an enlarged scale of the higher intensity diffraction peaks of the prepared samples (2θ range: 30–38°) is shown at the outset of Figure 1 and reveals a slight shift towards higher 2θ as the concentration of Te^{2-} (ionic radius 207 pm) increases, which has been attributed to Te's larger ionic radius compared with that of Te. The crystal planes of rhombohedral LCO are marked in Figure 1 with reference to standard JCPDS Card No. 48-0123. To understand the reduction in TeO_2, we took XRD for both parents and reduced Te, which is shown in Figure 2. TeO_2 is successfully reduced to Te, as shown by the XRD data, which is supported by the ICSD collection codes 34-422 and 65-3048 for TeO_2 and Te, respectively. The crystal structure transforms from tetragonal to hexagonal during the reduction of TeO_2 to Te, as reported in the reference datasheet. Table 1 illustrates the lattice parameter, crystal system, space group, and crystallite size of TeO_2, Te, LCO, 2.5% Te-LCO, and 5% Te-LCO. The average crystal size was determined using the Debye–Scherrer formula and the lattice parameters were determined using unit cell software [Name: Unit cell win, Version CCP14].

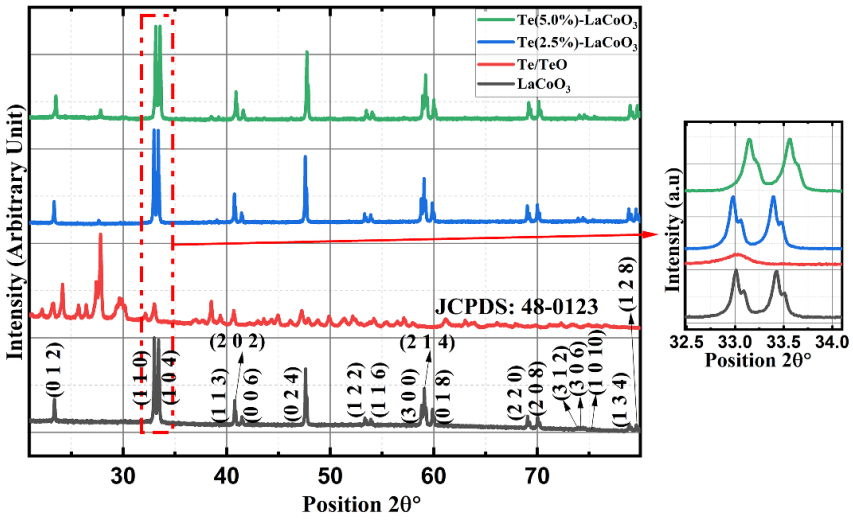

Figure 1. X-ray diffraction of LCO, Te, and Te (2.5% and 5%)-LCO. Outset shows the magnified image of high-intensity peaks of LCO, Te, and Te (2.5% and 5%)-LCO.

Table 1. The crystallite size and lattice parameter of TeO_2, Te, LCO, LCO/Te (2.5%), and LCO/Te (5%).

Composition	Crystal System	Space Group	Crystallite Size (nm) $D=\frac{0.9\lambda}{\beta\cos\theta}$	Lattice Parameter (Å)		
				a	b	c
TeO_2	Tetragonal	$P4_12_12$	26.80514	5.40681	5.40865	13.20149
Te	Hexagonal	$P3_121$	28.33724	4.19097	4.19123	5.98099
$LaCoO_3$	Rhombohedral	$R\bar{3}c$	43.42469	5.41768	5.39366	13.13084
2.5% Te/LCO	Rhombohedral	$R\bar{3}c$	31.59925	5.42428	5.39256	13.1579
5% Te/LCO	Rhombohedral	$R\bar{3}c$	31.59925	5.42681	5.39434	13.20149

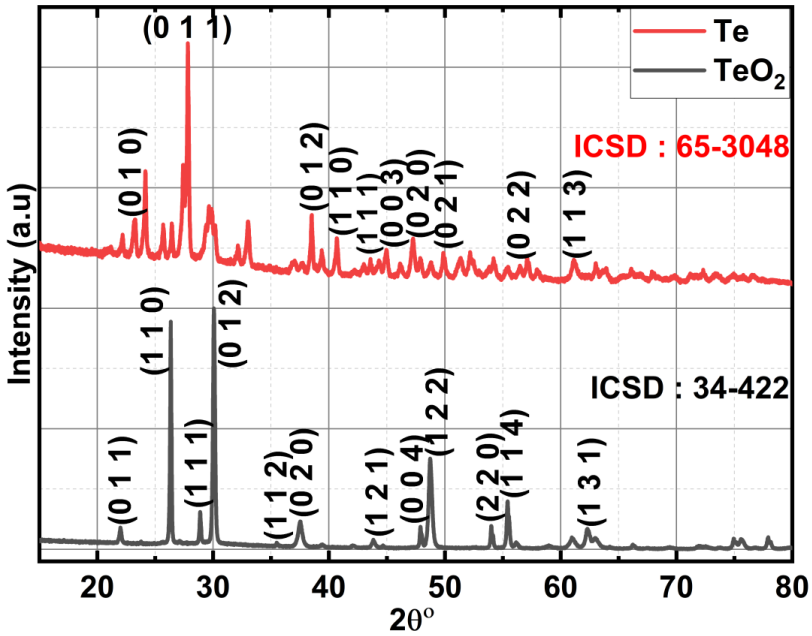

Figure 2. X-ray diffraction of TeO_2 and Te.

2.2. Raman Spectrum Analysis of Te-Incorporated $LaCoO_3$

Hydrothermally produced LCO, chemically reduced Te, and Te-impregnated LCO are analysed for their chemical distribution using Raman spectroscopy. In Figure 3, Raman scattering measurements of LCO, Te, 2.5% Te-LCO, and 5% Te-LCO are displayed. The primeval LCO has weak Raman signals compared to Te, 2.5% Te-LCO, and 5% Te-LCO, whereas the 2.5% and 5% Te in cooperated LCO have good Te signals, which match the Te and have a slight shift and have a significant Raman characteristic peak. The Co-O-Co stretching mode in strongly deformed CoO_6 may be related to the newly widened band at 516 cm^{-1} [27]. The E_g symmetry, which may be related to exterior mode (La-O) vibration, is responsible for the 116 and 140 cm^{-1} peaks [28,29]. Te exhibits strong Raman-active phonon modes as a result of its high atomic number and electronic polarizability. Three atoms make up each tellurium unit cell, which is arranged in an unending chain parallel to the c-axis. One A_1 mode and two degenerate E modes, which are identified by rigid-chain rotation across the a- and b-axes and which fit into the Te lattice's D_3 symmetry group, are indicated by the Raman spectra. The week bands at 103 cm^{-1} are attributed to the $E_{(1)}$ modes, which are responsible for the Raman spectra's $E_{(1)}$ bands. The $E_{(2)}$ mode, which is primarily distinguished by asymmetries along the c-axis, corresponds to the bands at 141 cm^{-1}. The broad bands are of the second order at 268.9 cm^{-1} [30–32]. Tellurium's characteristic peaks at 122 and 141 cm^{-1} can be seen in both 2.5% Te-LCO and 5% Te-LCO, which corresponds to the A_1 bond-stretching mode and two degenerate E bond-stretching modes, respectively [33]. There is a slight red shift for the high-intensity Te peak in Te-LCO, and increasing the Te concentrations broadens the peaks.

2.3. SEM and Energy-Dispersive X-ray (EDS) Analysis of Te-Incorporated $LaCoO_3$

Te-LCO composites are created by impregnating tellurium into the pores of LCO, which successfully preserves the material's irregular spherical shape. Figure 4a–e presents the surface morphology of TeO_2, Te, LCO, 2.5% Te-LCO, and 5% Te-LCO, respectively. TeO_2 and Te show (Figure 4a,b) that the reduction leads to the uniformly distributed plated nanostructure from mono-dispersed irregular microcrystals of about a few micrometers to nearly 500 nm. The hydrothermal synthesis of LCO (Figure 4c) leads to a well-dispersed spherical crystallite structure and the impregnating of Te in LCO (Figure 4d,e) has impacted slightly on the microstructure. The Te-impregnated LCO is well segregated, which is visible

in the SEM micrograph. The EDAX spectrum of TeO_2, Te, LCO, 2.5% Te-LCO, and 5% Te-LCO is revealed in Figure 4, which confirms the occurrence of constituent elements.

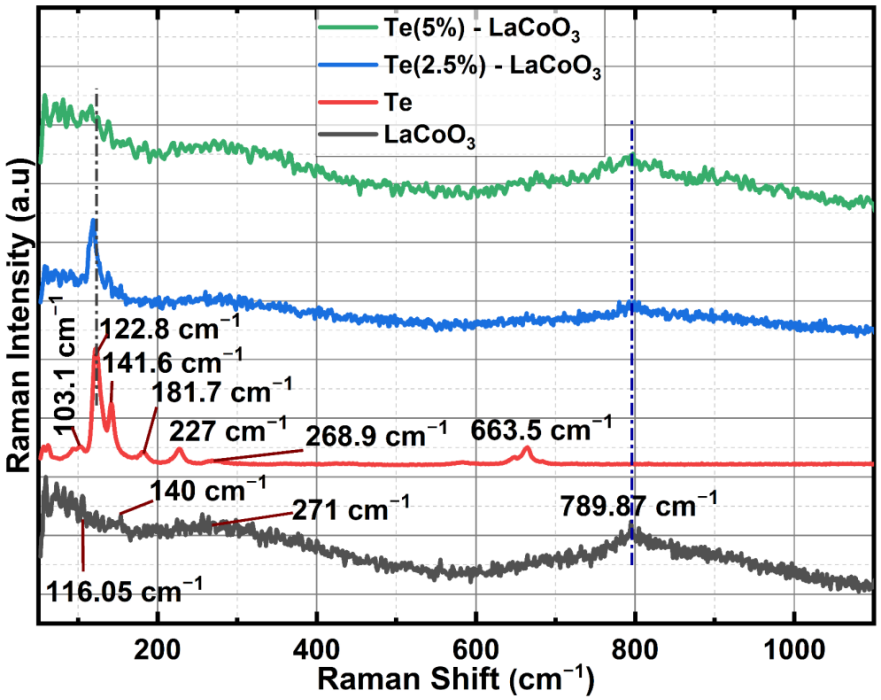

Figure 3. Raman spectroscopy of LCO, Te, 2.5% Te-LCO, and 5% Te-LCO.

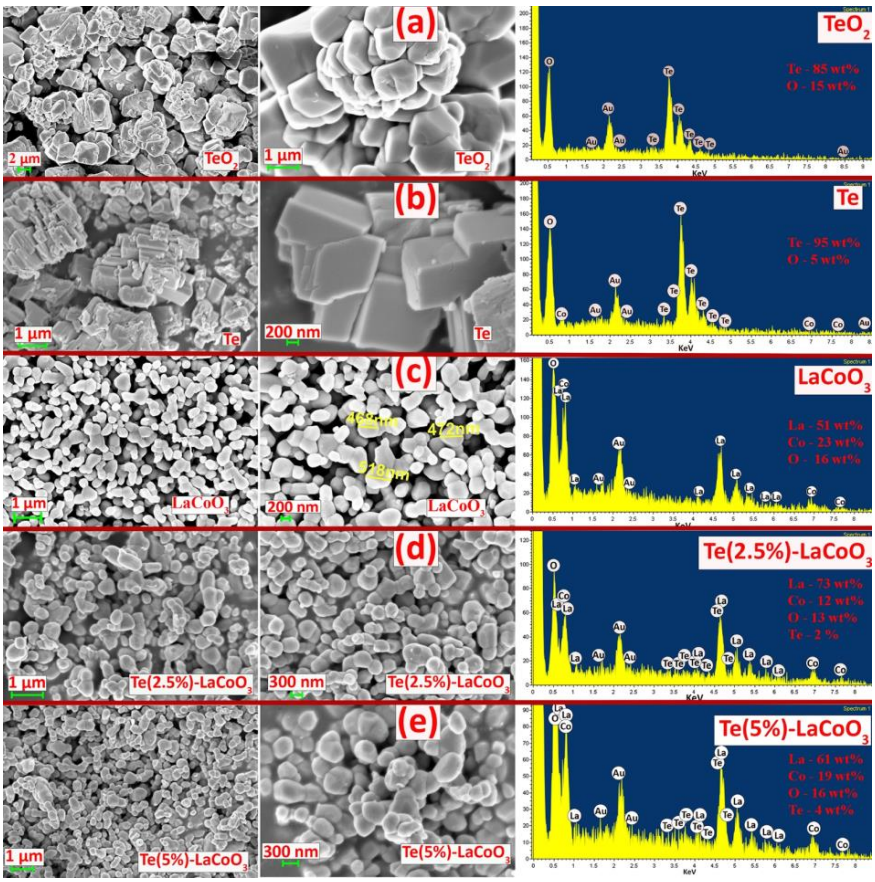

Figure 4. SEM and EDAX image of (**a**) TeO_2, (**b**) Te, (**c**) $LaCoO_3$, (**d**) Te (2.5%)-LCO and (**e**) Te (5%)-LCO.

2.4. X-ray Photoelectron Spectroscopy (XPS) Studies of Te-Incorporated $LaCoO_3$

X-ray photoelectron spectroscopy (XPS) is utilised to investigate the valence state of pure LCO and Te in-cooperated LCO with a Te content of 5 wt.%. The XPS survey spectra in Figure 5a,d demonstrate the presence of Co, O, La, and Te (5 wt.% Te in-cooperated LCO). Core-level XPS spectra verify the real valence states of the individual components. Co 2p core level spectra, both pure and Te in-cooperated, are shown in Figure 5c,f, respectively. LCO's two asymmetric peaks are located at 780.18 and 795.45 eV and are most similar to those of Co $2p_{3/2}$ and Co $2p_{1/2}$. Paramagnetic Co^{2+} is formed at the surface, accounting for the visible satellite peaks above the primary photo peaks [34]. Because of the presence of numerous excitations and the coexistence of Co^{3+} and Co^{2+} states, the Co 2p peak expanded and shifted toward higher energy when Te was present in conjunction with LCO. The existence of both high-spin Co^{2+} and low-spin Co^{3+} ions was further validated by the appearance of the Co $2p_{3/2}$ peaks at 781.23 eV with decreased satellite peaks [35,36]. The Co 2p photoelectron spectra of Te-LCO are chemically shifted sufficiently to permit chemical identification. The Co $2p_{3/2}$ and Co $2p_{1/2}$ lines for Te-LCO were chemically shifted to 1.05 eV and 1.14 eV, respectively, to higher binding energies than for LCO. The Co $2p_{3/2}$ has diminished satellite peak may be due to the good exposure of LCO when we mechanically ball mill with Te, which leads to further oxidation of the samples towards the surface. According to research by Frost and colleagues [34,37], photoelectron spectra of high-spin Co^{2+} compounds show robust satellites, while those of low-spin Co^{2+} compounds either show weak satellites or none at all. Te-LCO has a core photoemission peak separation of 15.36 eV, while LCO's is 15.27 eV. These values are fairly close to the CoO and Co_3O_4 values that have previously been published [34,38] as depicted in Figure 5. As anticipated, the La 3d line shows the four component peaks (Figure 5b,e). According to our prior research [19], La $3d_{5/2}$ and La $3d_{3/2}$ are associated with the double peaks of LCO, which emerge at 834.7 and 838.34 eV, respectively. These peaks can be attributed to the La^{3+} state and represent charge transfer between the La_2O_3, O2p, and La4f orbits [36–41] or substantial electronic configuration final state mixing [42]. Te in-corporation causes a shift toward greater binding energies, indicating that the lattice structure is being destroyed. Because of Te's multi-valence state, the additive peak with the highest intensity at 837.34 eV could be attributable to the synthesis of La sub-oxide (La-O_x). The observed core-level Te 3d spectra have been deconvoluted into single $3d_{3/2}$ and $3d_{5/2}$ spin-state peaks at about 587 and 576 eV, respectively, to help explain it better. The chemical shift seen at Te $3d_{5/2}$ of approximately 3 eV towards higher binding energy from Te^{2-} is characteristic of $NaBH_4$-reduced TeO_2, which may form some surface oxidation layers (Te^0). Figure 5i shows the two asymmetric peaks of high-resolution Te 3d XPS spectroscopy, which reveals the $Te^{4+}/Te^{2-}/Te^0$ oxidation state for the $NaBH_4$-reduced TeO_2. The binding energy difference between $3d_{3/2}$ and $3d_{5/2}$ is 10.4 eV, which agrees with the literature [43–45]. As was previously mentioned, the presence of Te at high oxidation states reconstructs the crystal structure and produces more Co^{2+} and Co^{3+} at various spin states, which leads to additional defects. The perovskite's A and B sites are both affected by the equally distributed Te^{4+}, which results in an increase in the amount of La^{2+} in the A site and anisotropic Co^{2+} in the B site to balance the charge. As a result, the magnetic state of the perovskite LCO was affected by the discrete La 3d and Co 2p photoemission peaks that the 5% Te in-corporated LCO displayed at various spin states [46,47]. The same O 1s peaks associated with the LCO and 5% Te-LCO provide evidence that Te played a part in the incorrect perovskite oxide formation. As demonstrated in Figure 5, both the pristine and Te-LCO O 1s peaks had three unique peaks (h and g). O 1s peaks were observed at 528.8, 530.9, and 532.6 eV on the LCO surface. This major signal at 528.8 eV can be attributable to either bulk oxide or lattice oxygen (O^{2-}), which is in line with the findings from earlier studies [41]. When looking at the oxide system, the broad peaks that have greater binding energies are the ones that are the most challenging to interpret. The value of 530.9 eV can be explained by the presence of chemisorbed oxygen (O^-) or adsorbed H_2O/OH^- species, both of which create a vacancy at the surface for oxygen to occupy [48]. O 1s XPS spectra of the Te-impregnated LCO

surface show that superoxide (O^{2-}) formation occurs at a peak energy of 532.6 eV, while the other two peaks can be attributed to lattice oxygen, chemically adsorbed oxygen species on the oxygen vacancies, and physically adsorbed oxygen species on the surface. Three peaks with centres at BE = 529.5, 531.6, and 532.7 eV were revealed by deconvolution of the Te-impregnated LCO asymmetric O 1s spectra (Figure 5g) [49]. These peaks correspond to lattice oxygen (such as O_2), chemically adsorbed oxygen (such as O^-), and physically adsorbed oxygen (H_2O and O_2), respectively. This encourages the conception of more peroxide/superoxide ions, which results in the acquisition of stronger peaks at 532.7 eV. Te^{4+} is in higher oxidation states in the Te in-corporated LCO as a result of the exchange of oxygen species that occurs as oxygen vacancies form between bulk and surface oxides [40].

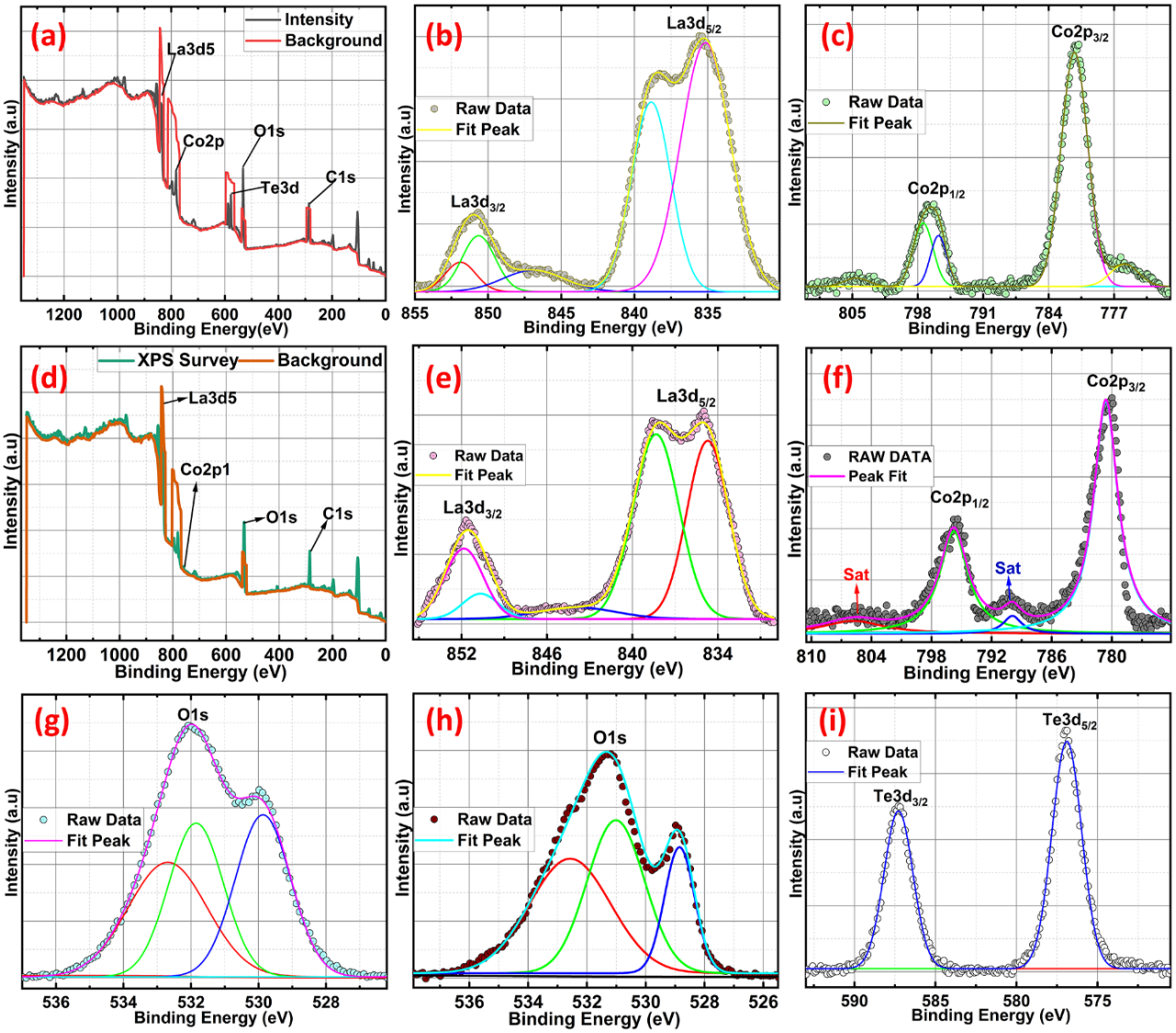

Figure 5. XPS survey scan (**a**,**d**) of LCO and Te (2.5%)-LCO, respectively. Detail XPS scan of La 3d (**b**,**e**), Co 2p (**c**,**f**), O 1s (**g**,**h**) of LCO and Te (2.5%)-LCO, respectively, and Te 3d (**i**) of Te (2.5%)-LCO.

2.5. Magnetic Properties of Te-Incorporated $LaCoO_3$

At 300 K, the field dependency of magnetization (M-H) for pristine LCO, 2.5% Te-LCO, and 5% Te-LCO was measured for a field change from −2.5 T to 2.5 T. The M-H loop at 300 K (Figure 6a) suggests that the samples are originally in a paramagnetic state (LCO) and that the magnetic state changes to a weak ferromagnetic with the addition of Te, as shown in Figure 6a, where the hysteresis develops with Te impregnation of LCO. When compared to the parent LCO, the overall magnetization value of the incubated samples is

lower. The samples have a very low magnetic saturation (M_S) value after incorporation with Te. However, some previous studies relate the magnetic state to the anti-ferromagnetic exchange interaction in the samples [50], which arises from the antiferromagnetically ordered localized high spin states present in these systems with the incorporation of Te [51]. The values of magnetization (M_S), M_R and H_C extracted from the magnetic data (Figure 6), are given in Table 2. With the initial incorporation of 2.5% Te, it induces coercivity and it decreases for higher concentrations of Te (5%). The anti-symmetric exchange interaction arises from the interaction of low spin Co (III) with the excited high spin Co (III). This further influences magnetocrystallite anisotropy and reduces the coercive field [52–55]. In our previous study of Mn-doped LCO, the RT M-H shows only a paramagnetic state even after incorporation with Mn at the Co site [19]. From the XPS study, it can be understood that the different valence states of Te may occupy La/Co sites, which enhances the magnetic property in the present LCO system.

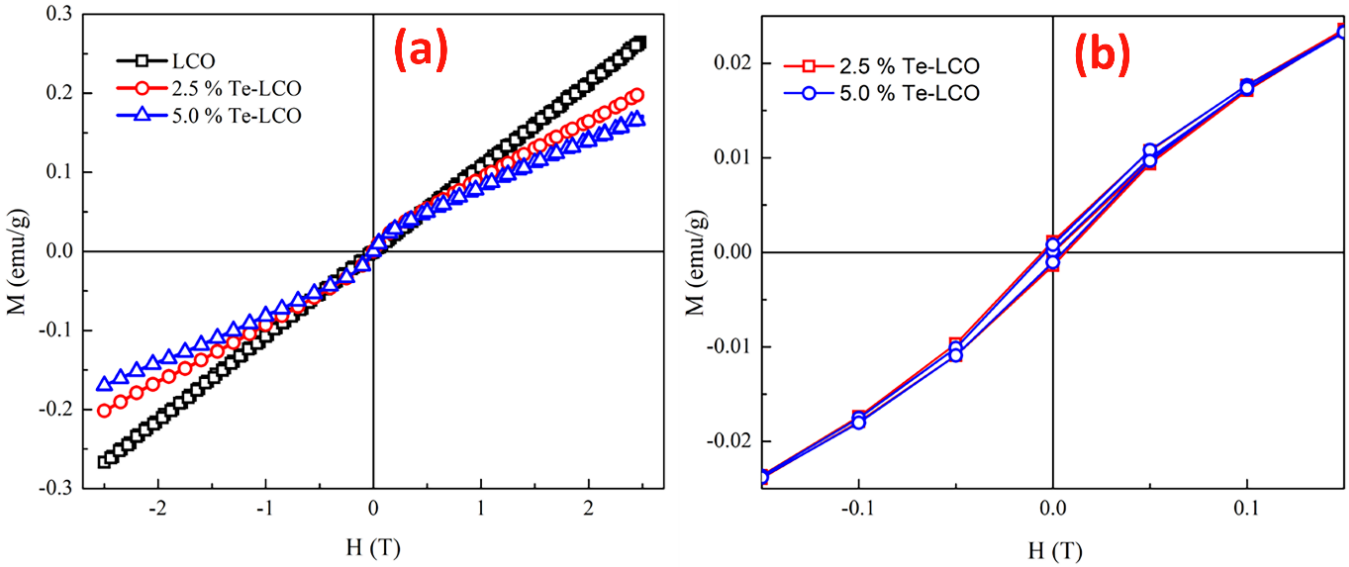

Figure 6. Isothermal magnetization curve of (**a**) LCO, 2.5% Te-LCO, and 5% Te-LCO at RT, and (**b**) enlarged image of LCO, 2.5% Te-LCO, and 5% Te-LCO at RT.

Table 2. Saturation magnetization (M), remnant magnetization (M_r), and coercivity (H_C) of pure and Te@LCO.

Composition	H_C (T)	M (emu/g) @300 K	M_r (emu/g)
LCO	--	---	-----
2.5% Te-LCO	0.0065	0.20166	0.00128
5% Te-LCO	0.0049	0.17051	0.00094

2.6. Transmission Analysis of Te-Incorporated $LaCoO_3$

Furthermore, TEM was used to verify the nanoparticle size and material structure. LCO Figure 7a,b, 2.5 wt.% Te-LCO (Figure 7d,e) and 5 wt.% Te-LCO (Figure 7g,h) demonstrate an evident ellipsoid structure with a 100–200 nm distribution in Figure 7. Due to the low Te concentration in LCO, lattice plane separation cannot be observed. In addition, Figure 7 shows the 5% Te-LCO's selected area electron diffraction (SAED) patterns. The composite reflected a single crystal structure with a few irregular brilliant spots, showing that the addition of Te affected the original structure of LCO [56]. Figure 7 depicts the interplanar spacing (d_{hkl}) measured from the SAED patterns.

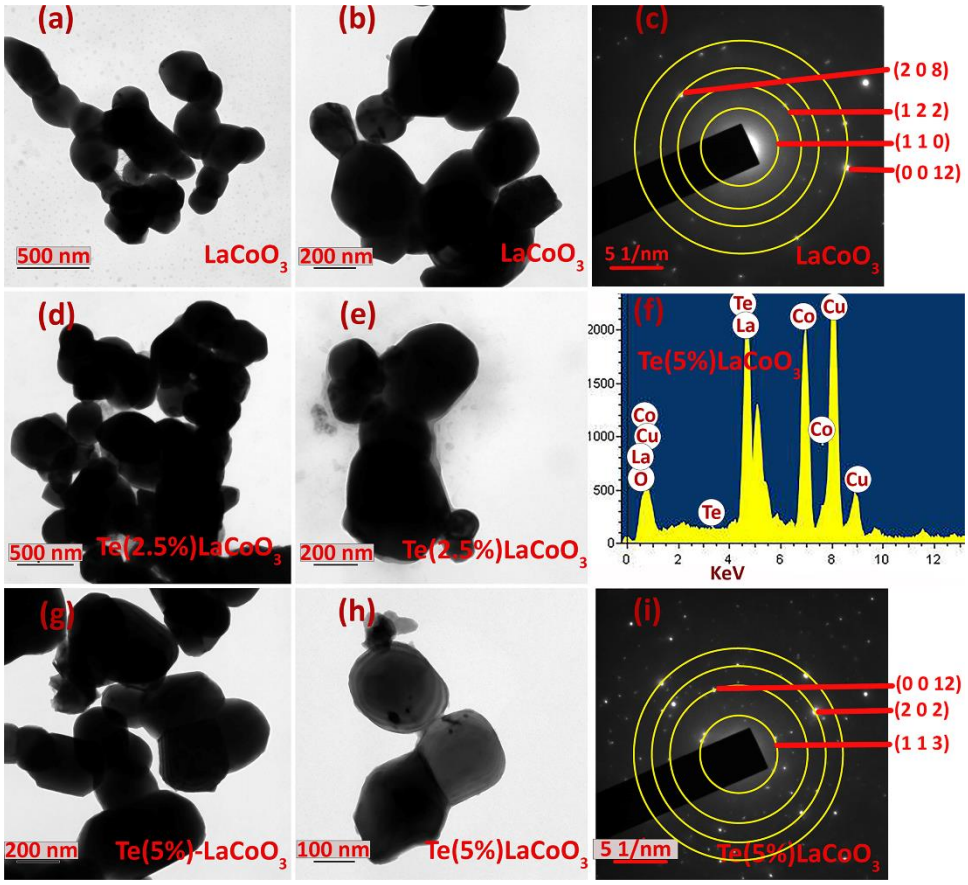

Figure 7. TEM image of (**a**,**b**) LaCoO3; (**d**,**e**) Te (2.5%) LCO; and (**g**,**h**) Te (5%) LCO. SAED of (**c**) $LaCoO_3$ and (**i**) Te (5%) LCO and EDS image of (**f**) Te (5%) LCO.

3. Materials and Methods

3.1. Materials

3.1.1. Materials for the Preparation of Te (Method 1)

The precursor materials used for the preparation of Te are Tellurium dioxide (TeO_2) (Sigma-Aldrich, Germany), and sodium borohydride ($NaBH_4$) (Merck, USA).

3.1.2. Materials for the Preparation of $LaCoO_3$ (Method 2)

The precursor materials used for the preparation of LCO are Lanthanum (III) nitrate hexahydrate ($La(NO_3)_3$ $6H_2O$) (Merck), cobalt (II) nitrate hexahydrate ($Co(NO_3)_2$ $6H_2O$) (Merck), ammonia solution about 25% (NH_4OH) (Merck), and sodium hydroxide (NaOH) (Merck).

3.1.3. Materials for the Preparation of Te (2.5%)-Impregnated $LaCoO_3$ and Te-(5%) Impregnated $LaCoO_3$ (Method 3)

The materials obtained after the preparation of method 1 and method 2 are Te and $LaCoO_3$. These two materials are used to prepare Te-impregnated $LaCoO_3$. All of the chemicals are reagent grade with high purity (99.9%) and can be used straight out of the package.

3.2. Methods

3.2.1. Method 1: The Preparation of Te

From room temperature (RT) to boiling point (BP), 100 mL of $C_2H_6O_2$ and TeO_2 (2 g wt.) were homogenously mixed using a magnetic stirrer in a silicon oil bath to maintain a temperature of 180 °C in a double-neck round-bottomed flask equipped with a reflux

cooler for 2 h or longer. The ratio of salt to reductant was maintained at 1:4. After 2 h, 8 g of $NaBH_4$ was added slowly into the mixture with the evolution of gases. While introducing $NaBH_4$, regular personnel protective equipment (PPE) precautions and other safety measures were taken. After adding the reducing agent, the reaction mixtures were stirred for two hours and cooled to RT naturally. The ultimate precipitate was centrifuged and repeatedly washed with DI water, acetone, and ethanol before being dried at RT Equation, which represents the reaction of the sodium borohydride and tellurium dioxide (1).

$$TeO_2 + C_2H_6O_2 \xrightarrow{180\ ^\circ C||NaBH_4} TeO(OH) + \frac{1}{2}H_2^{\uparrow} + \frac{1}{2}B_2H_4 + NaOH \quad (1)$$

TeO (OH^-) is formed in two steps Equation (1) involves reduction by hydrogenation. Initially, TeO_2 was reduced to equivalent ions and hydrogenated oxygen (H^+O) was collected at the surface. The evolved H_2 may dissociate into H atoms or ions during the reduction process.

3.2.2. Method 2: The Preparation of $LaCoO_3$

We have briefly discussed the hydrothermal synthesis of LCO in our previous report [18].

3.2.3. Method 3: The Preparation of Te-Impregnated $LaCoO_3$

The third method is ball milling of the samples obtained from the first two methods. The ball-milling of Te and LCO is as follows: 2.5% and 5% Te are mixed with 97.5% and 95% LCO by weight, respectively, and well ground for 10 h with intervals of 30 min to avoid settling of powder on the sides of the ball-mill container. After the ball milling, the material is taken for further studies.

3.3. Characterisation Technique

To investigate the phase transformations at ambient temperatures, CuK-alpha radiation was utilised in an Empyrean Malvern Panalytical X-ray Powder Diffractometer. A field emission scanning electron microscope (FESEM) equipped with energy-dispersive X-ray spectroscopy (EDAX) was used to investigate the surface topography and composition of the microstructure. The vibrational modes of the materials are studied using a confocal micro-Raman microscope (WiTec Alpha 300, Germany) equipped with AFM imaging and a He-Ne laser as the excitation source (λ-exc = 532 nm) in a backscattering setup. In order to investigate the chemical composition of the surface, we used X-ray photoelectron spectroscopy (XPS) with Al K-alpha X-rays (Thermo Scientific, UK). A JEOL JEM 2100 HRTEM was utilised for microscopic examination and evaluation. The effect of a magnetic field strength of 5 T on the material's magnetization (M-H) at room temperature was investigated using SQUID-MPMS (Quantum Design, USA).

4. Conclusions

The findings provide a systematic examination of Te impregnation in LCO perovskite oxide at various concentrations. As-prepared perovskite oxides have been analysed for their magnetic properties and crystal structures. The results showed that the samples exhibited an imperfect rhombohedral crystal structure. Adding Te to LCO produces a perovskite with a high multi-valence state of $Te^{4+/2-}$ and three distinct oxygen species, which creates oxygen deficiency. Raman spectroscopy and XPS analysis both show that the presence of Te^{4+} prevents the formation of defective cobalt oxide. After being subjected to impact and iteration in a ball mill, the SEM micrograph of LCO and Te-impregnated LCO demonstrates the structural similarity between the parent and included samples. However, XRD analysis revealed that Te-LCO was successfully reduced and incorporated into the mixture as a result of the ball mill's influence on the crystallite structure. The structural integrity of the perovskite samples has also been verified using transmission electron microscopy investigation. The presence of weak ferromagnetic order at ambient

temperature after impregnation implies its potential application in magnetic devices and hypersonic vehicles.

Author Contributions: J.S.: Formal Analysis, Data Curation, Conceptualization and Writing—Original Draft; P.S.: Data Curation, Formal analysis, Conceptualization, Validation, Writing—Review and Editing; S.E.M.: Conceptualization, Data Curation, Formal Analysis, Supervision, Writing—Review and Editing and Proof Reading; I.K.: Data Curation, Supervision, Writing—Review and Editing, and Project administration; N.P.: Formal Analysis; V.E.: Formal Analysis. All authors have read and agreed to the published version of the manuscript.

Funding: This research was funded by the National Research Foundation of Korea (NRF) grant, funded by the Korean government (MIST) (No. 2022R1C1C1006414) and (No. 2021R1A4A1032207). The author SEM acknowledges the funding agency of the SERB-TARE fellowship (TAR/2021/000097).

Institutional Review Board Statement: Not applicable.

Informed Consent Statement: Not applicable.

Data Availability Statement: All the data used in the manuscript are within the manuscript.

Conflicts of Interest: The authors declare no conflict of interest.

References

1. Fist, N.; Dinan, J.; Stadelmann, R.; Orlovskaya, N. In situ three point bending device for measurements of vibrational response of ceramics under stress by microRaman spectroscopy. *Adv. Appl. Ceram.* **2012**, *111*, 433–439. [CrossRef]
2. Samantaray, C.B.; Sim, H.; Hwang, H. Electronic structure and optical properties of barium strontium titanate (BaxSr1−xTiO$_3$) using first-principles method. *Phys. B Condens. Matter* **2004**, *351*, 158–162. [CrossRef]
3. Samantaray, C.B.; Sim, H.; Hwang, H. The electronic structures and optical properties of BaTiO$_3$ and SrTiO$_3$ using first-principles calculations. *Microelectron. J.* **2005**, *36*, 725–728. [CrossRef]
4. Bednorz, J.G.; Müller, K.A. Sr1−xCaxTiO$_3$: An XY Quantum Ferroelectric with Transition to Randomness. *Phys. Rev. Lett.* **1984**, *52*, 2289–2292. [CrossRef]
5. Frederikse, H.P.R.; Thurber, W.R.; Hosler, W.R. Electronic Transport in Strontium Titanate. *Phys. Rev.* **1964**, *134*, A442–A445. [CrossRef]
6. Koonce, C.S.; Cohen, M.L.; Schooley, J.F.; Hosler, W.R.; Pfeiffer, E.R. Superconducting Transition Temperatures of Semiconducting SrTiO$_3$. *Phys. Rev.* **1967**, *163*, 380–390. [CrossRef]
7. Wang, H.; Wang, B.; Li, Q.; Zhu, Z.; Wang, R.; Woo, C.H. First-principles study of the cubic perovskitesBiMO$_3$(M=Al, Ga, In, and Sc). *Phys. Rev. B* **2007**, *75*, 245209. [CrossRef]
8. Baettig, P.; Schelle, C.F.; LeSar, R.; Waghmare, U.V.; Spaldin, N.A. Theoretical Prediction of New High-Performance Lead-Free Piezoelectrics. *Chem. Mater.* **2005**, *17*, 1376–1380. [CrossRef]
9. Muta, H.; Kurosaki, K.; Yamanaka, S. Thermoelectric properties of rare earth doped SrTiO$_3$. *J. Alloys Compd.* **2003**, *350*, 292–295. [CrossRef]
10. Sivaprakash, P.; Divya, S.; Parameshwari, R.; Saravanan, C.; Sagadevan, S.; Arumugam, S.; Muthu, S.E. Influence of Zn^{2+} doping towards the structural, magnetic, and dielectric properties of NiFe$_2$O$_4$ composite. *J. Mater. Sci. Mater. Electron.* **2020**, *31*, 16369–16378. [CrossRef]
11. Millis, A.J.; Shraiman, B.I.; Mueller, R. Dynamic Jahn-Teller Effect and Colossal Magnetoresistance inLa1−xSrxMnO$_3$. *Phys. Rev. Lett.* **1996**, *77*, 175–178. [CrossRef]
12. Divya, S.; Sivaprakash, P.; Raja, S.; Muthu, S.E.; Eed, E.M.; Arumugam, S.; Oh, T.H. Temperature-dependent dielectric and magnetic properties of NiFe$_2$O$_4$ nanoparticles. *Appl. Nanosci.* **2021**, *13*, 1327–1336. [CrossRef]
13. Dragan, M.; Enache, S.; Varlam, M.; Petrov, K. Perovskite-Type Lanthanum Cobaltite LaCoO$_3$: Aspects of Processing Route toward Practical Applications. In *Cobalt Compounds and Applications*; IntechOpen: London, UK, 2019. [CrossRef]
14. Hilgenkamp, H.; Ariando, A.; Smilde, H.-J.H.; Blank, D.H.A.; Rijnders, G.; Rogalla, H.; Kirtley, J.R.; Tsuei, C.C. Ordering and manipulation of the magnetic moments in large-scale superconducting π-loop arrays. *Nature* **2003**, *422*, 50–53. [CrossRef]
15. Raccah, P.M.; Goodenough, J.B. First-Order Localized-Electron ⇆ Collective-Electron Transition in LaCoO$_3$. *Phys. Rev.* **1967**, *155*, 932–943. [CrossRef]
16. Rodríguez, M.A.S.; Goodenough, J. Magnetic and Transport Properties of the System La$_{1-x}$Sr$_x$CoO$_{3-\delta}$ ($0 < x \leq 0.50$). *J. Solid State Chem.* **1995**, *118*, 323–336. [CrossRef]
17. Maignan, A.; Flahaut, D.; Hebert, S. Sign change of the thermoelectric power in LaCoO$_3$. *Eur. Phys. J. B* **2004**, *39*, 145–148. [CrossRef]
18. Guo, E.-J.; Desautels, R.; Keavney, D.; Roldan, M.A.; Kirby, B.J.; Lee, D.; Liao, Z.; Charlton, T.; Herklotz, A.; Ward, T.Z.; et al. Nanoscale ferroelastic twins formed in strained LaCoO$_3$ films. *Sci. Adv.* **2019**, *5*, eaav5050. [CrossRef]

19. Sahadevan, J.; Radhakrishnan, M.; Padmanathan, N.; Muthu, S.E.; Sivaprakash, P.; Kadiresan, M. Effect of Mn substitution on magnetic behaviour of oxygen defective $LaCoO_3$ perovskite oxide. *Mater. Sci. Eng. B* **2022**, *284*, 115875. [CrossRef]
20. Zhou, J.-S.; Yan, J.-Q.; Goodenough, J.B. Bulk modulus anomaly in $RCoO_3$(R = La, Pr, and Nd). *Phys. Rev. B* **2005**, *71*, 220103. [CrossRef]
21. Vogt, T.; Hriljac, J.A.; Hyatt, N.C.; Woodward, P. Pressure-induced intermediate-to-low spin state transition in $LaCoO_3$. *Phys. Rev. B* **2003**, *67*, 140401. [CrossRef]
22. Divya, S.; Sivaprakash, P.; Raja, S.; Muthu, S.E.; Kim, I.; Renuka, N.; Arumugam, S.; Oh, T.H. Impact of Zn doping on the dielectric and magnetic properties of $CoFe_2O_4$ nanoparticles. *Ceram. Int.* **2022**, *48*, 33208–33218. [CrossRef]
23. Xu, Y.; Zielke, P.; Van Nong, N.; Pirou, S.; Reolon, R.; Si, X.; Simonsen, S.B.; Norby, P.; Lühmann, H.; Bensch, W.; et al. Hydrothermal Synthesis, Characterization, and Sintering Behavior of Core-Shell Particles: A Principle Study on Lanthanum Strontium Cobaltite Coated with Nanosized Gadolinium Doped Ceria. *Ceramics* **2018**, *1*, 246–260. [CrossRef]
24. Ayyob, M.; Ahmad, I.; Hussain, F.; Bangash, M.K.; Awan, J.A.; Jaubert, J.-N. A new technique for the synthesis of lanthanum substituted nickel cobaltite nanocomposites for the photo catalytic degradation of organic dyes in wastewater. *Arab. J. Chem.* **2020**, *13*, 6341–6347. [CrossRef]
25. Deeksha; Kour, P.; Ahmed, I.; Haldar, K.K.; Yadav, K. Tuning the Morphology of Lanthanum Cobaltite Using the Surfactant-Assisted Hydrothermal Approach for Enhancing Oxygen Evolution Catalysis. In Proceedings of the National Workshop on Recent Advances in Condensed Matter and High Energy Physics; Springer Proceedings in Physics. Springer: Singapore, 2022; Volume 278, pp. 15–24. [CrossRef]
26. Tepech-Carrillo, L.; Escobedo-Morales, A.; Pérez-Centeno, A.; Chigo-Anota, E.; Sánchez-Ramírez, J.F.; López-Apreza, E.; Gutiérrez-Gutiérrez, J. Preparation of Nanosized $LaCoO_3$ through Calcination of a Hydrothermally Synthesized Precursor. *J. Nanomater.* **2016**, *2016*, 6917950. [CrossRef]
27. Popa, M. Characterization of LaMeO3 (Me: Mn, Co, Fe) perovskite powders obtained by polymerizable complex method. *Solid State Ionics* **2002**, *154–155*, 135–141. [CrossRef]
28. Iliev, M.N.; Abrashev, M.V. Raman phonons and Raman Jahn-Teller bands in perovskite-like manganites. *J. Raman Spectrosc.* **2001**, *32*, 805–811. [CrossRef]
29. Orlovskaya, N.; Steinmetz, D.; Yarmolenko, S.; Pai, D.; Sankar, J.; Goodenough, J. Detection of temperature- and stress-induced modifications of $LaCoO_3$ by micro-Raman spectroscopy. *Phys. Rev. B-Condens. Matter Mater. Phys.* **2005**, *72*, 014122. [CrossRef]
30. Martin, R.M.; Ucovsky, G.I.; Helliwell, K. Intermolecnlar bonding and lattice dynamics of Se and Te. *Phys. Rev. B-Condens. Matter Mater. Phys.* **1976**, *13*, 1383. [CrossRef]
31. Pine, A.S.; Dresselhaus, G. Raman Scattering in Paratellurite, TeO_2. *Phys. Rev. B-Condens. Matter Mater. Phys.* **1972**, *5*, 4087. [CrossRef]
32. Marini, C.; Chermisi, D.; Lavagnini, M.; Di Castro, D.; Petrillo, C.; Degiorgi, L.; Scandolo, S.; Postorino, P. High-pressure phases of crystallite tellurium: A combined Raman and ab initio study. *Phys. Rev. B-Condens. Matter Mater. Phys.* **2012**, *86*, 064103. [CrossRef]
33. He, J.; Lv, W.; Chen, Y.; Wen, K.; Xu, C.; Zhang, W.; Li, Y.; Qin, W.; He, W. Tellurium-Impregnated Porous Cobalt-Doped Carbon Polyhedra as Superior Cathodes for Lithium-Tellurium Batteries. *ACS Nano* **2017**, *11*, 8144–8152. [CrossRef]
34. Haber, J.; Ungier, L. On chemical shifts of ESCA and Auger lines in cobalt oxides. *J. Electron. Spectrosc. Relat. Phenom.* **1977**, *12*, 305–312. [CrossRef]
35. McIntyre, N.S.; Johnston, D.D.; Coatsworth, L.L.; Davidson, R.D.; Brown, J.R. X-ray photoelectron spectroscopic studies of thin film oxides of cobalt and molybdenum. *Surf. Interface Anal.* **1990**, *15*, 265–272. [CrossRef]
36. Wang, H.; Xu, W.; Richins, S.; Liaw, K.; Yan, L.; Zhou, M.; Luo, H. Polymer-assisted approach to LaCo1-xNixO_3 network nanostructures as bifunctional oxygen electrocatalysts. *Electrochim. Acta* **2019**, *296*, 945–953. [CrossRef]
37. DFrost, C.; McDowell, C.A.; Woolsey, I.S. Evidence for multiplet splitting of 2p photoelectron lines of transition metal complexes. *Chem. Phys. Lett.* **1972**, *17*, 320–323. [CrossRef]
38. Seim, H.; Nieminen, M.; Niinistö, L.; Fjellvåg, H.; Johansson, L.S. Growth of $LaCoO_3$ thin films from β-diketonate precursors. *Appl. Surf. Sci.* **1997**, *112*, 243–250. [CrossRef]
39. Ramana, C.V.; Vemuri, R.S.; Kaichev, V.V.; Kochubey, V.A.; Saraev, A.A.; Atuchin, V.V. X-ray photoelectron spectroscopy depth profiling of La_2O_3/Si thin films deposited by reactive magnetron sputtering. *ACS Appl. Mater. Interfaces* **2011**, *3*, 4370–4373. [CrossRef]
40. Jiang, X.; Dong, Y.; Zhang, Z.; Li, J.; Qian, J.; Gao, D. Cation substitution of B-site in $LaCoO_3$ for bifunctional oxygen electrocatalytic activities. *J. Alloys Compd.* **2021**, *878*, 160433. [CrossRef]
41. Armelao, L.; Barreca, D.; Bottaro, G.; Gasparotto, A.; Maragno, C.; Tondello, E. $LaCoO_3$ Nanosystems by a Hybrid CVD/Sol-Gel Route: An XPS Investigation. *Surf. Sci. Spectra* **2003**, *10*, 143–149. [CrossRef]
42. Vasquez, R.P. X-ray photoemission measurements of La1-xCaxCoO_3(x = 0, 0.5). *Phys. Rev. B-Condens. Matter Mater. Phys.* **1996**, *54*, 14938. [CrossRef]
43. Ricco, A.J.; White, H.S.; Wrighton, M.S. X-ray photoelectron and Auger electron spectroscopic study of the CdTe surface resulting from various surface pretreatments: Correlation of photoelectrochemical and capacitance-potential behavior with surface chemical composition. *J. Vac. Sci. Technol. A Vac. Surf. Film.* **1984**, *2*, 910–915. [CrossRef]

44. Christie, A.B.; Sutherland, I.; Walls, J.M. Studies of the composition, ion-induced reduction and preferential sputtering of anodic oxide films on $Hg_{0.8}Cd_{0.2}Te$ by XPS. *Surf. Sci.* **1983**, *135*, 225–242. [CrossRef]
45. Hidetaka, K.; Yoshihisa, Y. Ylide-Metal Complexes. XIV. An X-Ray Photoelectron Spectroscopic Study on Tellurium Complexes of Methylenetriphenylphosphorane. *Bull. Chem. Soc. Jpn.* **1988**, *61*, 2990–2992. [CrossRef]
46. Branford, W.; Green, M.A.; Neumann, D.A. Structure and ferromagnetism in Mn^{4+} spinels: $AM_{0.5}Mn_{1.5}O_4$ (A = Li, Cu; M = Ni, Mg). *Chem. Mater.* **2002**, *14*, 1649–1656. [CrossRef]
47. Thummer, K.P.; Chhantbar, M.C.; Modi, K.; Joshi, H. Effect of Mn^{4+} substitution on magnetic behaviour of cobalt ferrite. *Indian J. Phys.* **2005**, *79*, 41–45.
48. Liang, H.; Hong, Y.; Zhu, C.; Li, S.; Chen, Y.; Liu, Z.; Ye, D. Influence of partial Mn-substitution on surface oxygen species of $LaCoO_3$ catalysts. *Catal. Today* **2013**, *201*, 98–102. [CrossRef]
49. Xiao, P.; Zhu, J.; Li, H.; Jiang, W.; Wang, T.; Zhu, Y.; Zhao, Y.; Li, J. Effect of textural structure on the catalytic performance of $LaCoO_3$ for CO oxidation. *ChemCatChem* **2014**, *6*, 1774–1781. [CrossRef]
50. Schmidt, R.; Wu, J.; Leighton, C.; Terry, I. Dielectric response to the low-temperature magnetic defect structure and spin state transition in polycrystalline $LaCoO_3$. *Phys. Rev. B-Condens. Matter Mater. Phys.* **2009**, *79*, 125105. [CrossRef]
51. Tomiyasu, K.; Sato, M.; Koyama, S.I.; Nojima, T.; Kajimoto, R.; Ji, S.; Iwasa, K. Magnetic properties of electron-doped $LaCoO_3$. *J. Phys. Soc. Jpn.* **2017**, *86*, 094706. [CrossRef]
52. Gignoux, D.; De Lacheisserie, E.D.T.; Schlenker, M. *Magnetism: Materials and Applications*; Springer: New York, NY, USA, 2005.
53. Sivaprakash, P.; Nitthin Ananth, A.; Nagarajan, V.; Parameshwari, R.; Arumugam, S.; Jose, S.; Muthu, S.E. Role of Sm^{3+} dopant in the formation of $La_{(1-x)}Sm_xCrO_3$ solid state nanoperovskites–correlation of its augmented physical properties. *Mater. Chem. Phys.* **2020**, *248*, 122922. [CrossRef]
54. Sahadevan, J.; Sojiya, R.; Padmanathan, N.; Kulathuraan, K.; Shalini, M.G.; Sivaprakash, P.; Esakki Muthu, S. Magnetic property of Fe_2O_3 and Fe_3O_4 nanoparticle prepared by solvothermal process. *Mater. Today: Proc.* **2022**, *58*, 895–897. [CrossRef]
55. Sivaprakash, P.; Nitthin Ananth, A.; Nagarajan, V.; Jose, S.; Arumugam, S. Remarkable enhancement of $La_{(1-x)}Sm_xCrO_3$ nanoperovskite properties: An influence of its doping concentrations. *Mater. Res. Bull.* **2017**, *95*, 17–22. [CrossRef]
56. Wang, R.; Ye, C.; Wang, H.; Jiang, F. Z-Scheme $LaCoO_3$/g-C_3N_4 for Efficient Full-Spectrum Light-Simulated Solar Photocatalytic Hydrogen Generation. *ACS Omega* **2020**, *5*, 30373–30382. [CrossRef]